Analysis of the mechanical properties of a fibreglass reinforced flexible pipe (FGRFP)

Gao, Yifan; Bai, Yong; Cheng, Peng; Fang, Pan; Xu, Yuxin

Important note
To cite this publication, please use the final published version (if applicable).
Please check the document version above.

Analysis of the mechanical properties of a fibreglass reinforced flexible pipe (FGRFP)

Yifan Gao , Yong Bai , Peng Cheng , Pan Fang & Yuxin Xu

Published online: 23 Dec 2020.

Submit your article to this journal ⧉

Article views: 78

View related articles ⧉

View Crossmark data ⧉

Check for updates

Analysis of the mechanical properties of a fibreglass reinforced flexible pipe (FGRFP)

Yifan Gao[a], Yong Bai[a], Peng Cheng[a], Pan Fang[b] and Yuxin Xu[a]

[a]College of Civil Engineering and Architecture, Zhejiang University, Hangzhou, People's Republic of China; [b]Department of Maritime and Transport Technology, Delft University of Technology, Delft, The Netherlands

ABSTRACT

Fibreglass reinforced flexible pipe (FGRFP) is a kind of composite thermoplastic pipe serving as a preferred application in the field of oil transportation. This paper studies the mechanical behaviour of FGRFPs under pure bending by experimental, numerical and theoretical methods. Full-scale four-point bending tests are conducted and the curvature-bending moment relations of specimens are recorded. In the numerical simulation method (NSM), a detailed finite element model considering both material and geometric nonlinear behaviour is established, and the composite is defined as an orthotropic elastic-plastic material. Based on the Euler–Bernoulli beam theory, a simplified theoretical method (STM) is proposed to predict the ultimate bending moment. In the parametric study, a simple formula is introduced to modify STM to make it more accurate. Good agreements proves the reasonability of the proposed NSM and STM. Additionally, STM could make a contribution to engineers in terms of a concise and relatively accurate way in ultimate status analysis.

1. Introduction

Zero pollution is the goal especially in the remote offshore areas where equipment for pollution control response is either limited or challenging to mobilise. As a result, the improvements of bonded flexible pipe are primarily driven by environmental safety, at the same time, applied to offshore development where mobile offshore production unit (MOPU) are used (Northcutt 2000). Until 1989, there had been scarcely new development in bonded flexible pipe, but, this situation changed after the MOPS were introduced (Northcutt 2000). In 1959, the first use of bonded flexible marine hoses for offshore loading was in offshore Miri, Sarawak (Gibson 1989). After that, in the British sector of the North Sea, the first bonded flexible flowlines and risers were installed in 1988. From then on, flexible pipes were extensively applied in various engineering practices, such as oil transportation (Gibson 1989). As a kind of bonded flexible pipe, fibre reinforced flexible pipe (FRFP) is composed of two kinds of materials, fibre and resin or polyethylene (PE). Fibres usually including carbon, aramid, Kevlar and glass are used in reinforced layers due to their excellent tensile strength and modulus. Resins (used as matrix in the reinforced layers), on the other hand, are capable of transferring stress among fibres, hence, enables the fibres inside the reinforced layers work together. However, Kevlar and carbon fibre are not usually used in deep-sea pipelines because of high cost and electrochemical corrosion (Xu et al. 2019). Recently, FGRFP becomes a favourable choice for its high corrosion resistance, light-weight characteristic, and relatively low fabrication and facility cost.

The cross section of the FGRFP studied in this paper, shown in Figure 1, consists of a polyethylene liner, eight layers

of reinforcement and an outer polyethylene coating. The inner liner pipe is made of ultra-high molecular weight polyethylene (UHMWPE), and the outer coating pipe is high-density polyethylene (HDPE). The reinforcement considered here is produced by the helical tape wrapping method, using prepreg tapes (shown in Figure 2) in which impregnated twisted glass fibres are embedded in the HDPE matrix. Since the twisted glass fibres are impregnated firmly, there is enough bonding between the fibres and the matrix. This is the main difference between FGRFP and other reinforced thermoplastic pipe (RTP) (Kruijer et al. 2005).

PE, the crucial part of FGRFP, exhibits a complicated characteristic, which comprises elasticity, plasticity, and viscosity, and its behaviours are also strongly dependent on temperature, time, and loading conditions. Many works have been done to investigate the non-linear behaviour of PE by using experimental and theoretical methods (Bodner 1987; Zhang and Moore 1997a, 1997b; Colak and Dusunceli 2006). Nevertheless, some simple models are widely used among the analysis of bonded flexible pipe. In the work of Kruijer et al. (2005), PE was treated as a linear elastic material in the analysis of RTP's reinforced layers. By using a linear elastic material model, Dhar and Moore (2006) made an investigation on the evaluation of local bending in profile-wall PE pipes. Zheng et al. (2006) and Li et al. (2009) also considered HDPE as a linear elastic material in analysing the properties of PSP (plastic pipe reinforced by cross-winding steel wire). In the investigation, made by Fang et al. (2018), on mechanical behaviour of FGRFPs under torsion, matrix made of HDPE in reinforced layers was treated as a linear elastic material both in theoretical model and finite element model. Fredriksson et al. (2007), who had made some improvements on simplification
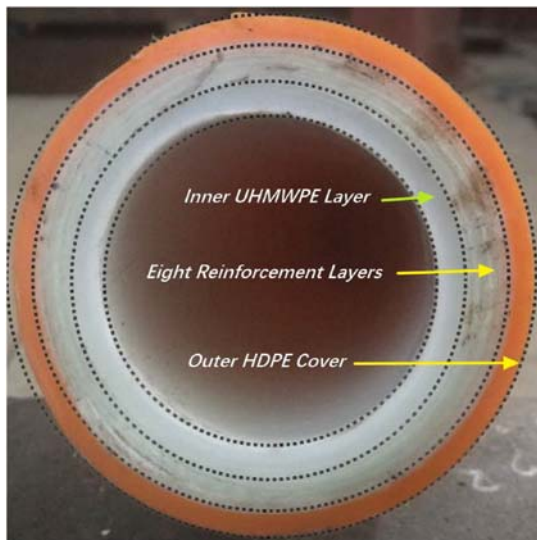
Figure 1. Structure of the FGRFP.

of HDPE material model, modelled the HDPE as an elastic-perfectly-plastic material to analysis the HDPE plastic net pens.

Regarding the greater complication of the reinforced layers, the classical laminated-plate theory has been adopted in most studies. In recent ten years, the classical laminated-plate theory has been adopted in most studies on the mechanical properties of reinforced layers of bonded flexible pipe (Xia et al. 2001; Zhu 2007; Menshykova and Guz 2014; Hu et al. 2015; Xing et al. 2015; Fang et al. 2018). It is remarkable that Menshykova and Guz (2014) proposed a theoretical method in analysing the multi-layer thick-wall composite pipe under bending, in which composite tube bending stiffness calculation equations proposed are of reference to this paper. In the classical laminated-plate theory, the reinforced layers are considered as an integral part which is merged by matrix and fibres or steel wires. Each reinforced layer is regarded as a 3D orthotropic cylinder, and the stiffness of the reinforced layer is determined by the rule of mixture. Nevertheless, rather than considering the elastic–plastic properties, the classical laminated-plate

theory assume that the material of reinforced layers is elastic. Therefore, the elastic–plastic mechanic behaviour of the bonded flexible pipe is not captured among those works. On the other hand, the embedded elements technique, which is used to account for the fact that the reinforcement plies and the coil are embedded into the matrix, is employed to investigate the non-linear behaviour of bonded flexible pipes in the commercial software Abaqus™ (Bai et al. 2013; Tonatto et al. 2016; Tonatto et al. 2017, 2018). After that, Fang et al. (2018) proposed a finite element model in which the glass fibre reinforcement was considered as an integral part, and the material orientation assignment technique was used to analyze the linear behaviour of FGRFP under torsion in the Abaqus™. Recently, Edmans et al. (2019) provided a multi-scale methodology in analysing the flexible pipe under bending load, which is innovative in the area of numerical simulation of risers.

In this paper, a uniaxial tensile test of both HDPE and UHMWPE is conducted to obtain the non-linear behaviour of PE used in the FGRFP specimens. Then, an experimental study of the FGRFP in a typical four-point bending test is presented. Curvature-bending moment relations were recorded during the test. In the numerical simulation method (NSM), a detailed finite element model (FEM) considering both material and geometric nonlinear behaviour is established to investigate the non-linear behaviour of the FGRFP by using a modified material orientation assignment technique. The composite in the reinforced layer is defined as an orthotropic elastic–plastic material, meanwhile, the inner and outer layer is regarded as an isotropic elastic–plastic material. The result of NSM shows excellent agreement with the experiments. Besides, a simplified theoretical method (STM) based on the Euler–Bernoulli beam theory is proposed to predict the ultimate moment of the FGRFP under pure bending. By modifying the classical laminated-plate theory, the STM takes the non-linear behaviour of both reinforced layers and inner and outer layers into consideration. This simplified method only takes into consideration the axial tangent module's contribution to the ultimate bending moment. The double integral method is applied to solve the equilibrium equations in the Matlab™. Then, a factor is introduced to modify STM, as STM does not consider the effect of geometric non-linearity in the cross section, unlike NSM. After that, a simple formula is used to calculate the factor which is obtained by the linear fitting method. The modified STM shows great agreement with NSM and the experiment, which proves the applicability of STM. Furthermore, a detailed parametric study on the structural response is conducted by using STM and NSM. Meanwhile, based on the ultimate curvature calculated by NSM, a simple formula of the ultimate curvature is proposed by using the surface fitting method. Finally, a profound understanding of the function of the FGRFP can be achieved, which can provide valuable advice for this kind pipe's design and application.

2. Experiment

2.1. Material experiments

Aiming at evaluating the mechanical characteristics of the HDPE and UHMWPE used in this pipe, uniaxial tensile tests are conducted by an electronic universal testing machine.


Figure 2. Prepreg tape of the FGRFP.

According to the stander ISO527-2012 (ISO 2012), the HDPE and UHMWPE are made into the dumb-bell shape, and the elastic modulus of them is calculated as the secant modulus when the true strain is between 0.05% and 0.25%.

After the material test, the engineering stress–strain data can be downloaded from the computer of the electronic universal testing machine. Then, the engineering stress–strain data is reshaped into the true stress–strain data, and the obtained curves are shown in Figure 3. From Figure 3, it can be observed that the stress of the HDPE begins to level off when the strain is over 7%~10%. It means that the HDPE begins to lose its axial tensile strength for axial strains higher than these values.

The mechanical characteristics data of fibre-glass shown in Table 1 are provided by the manufacturer of the pipe.

2.2. Experiments of the pipe

The bending experiment is usually known as the three-point bending test and the four-point bending test. Troina et al. (2003) used a bending test, in which the flexible pipe was regarded as a cantilever beam, and the bending stiffness of the specimen can be measured by applying a displacement on the end of the beam. Kagoura et al. (2003) employed the three-points bending test to investigate the bending stiffness
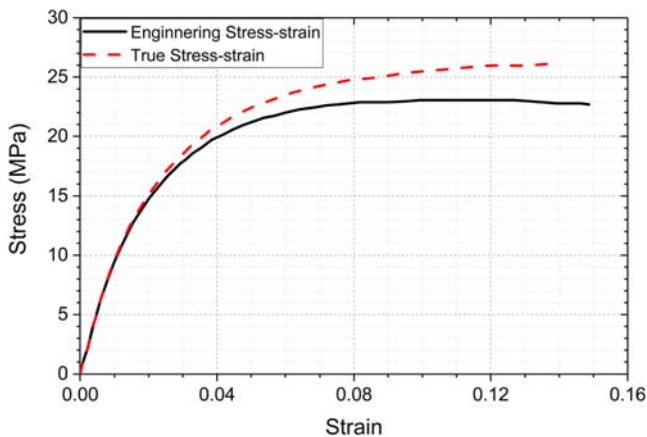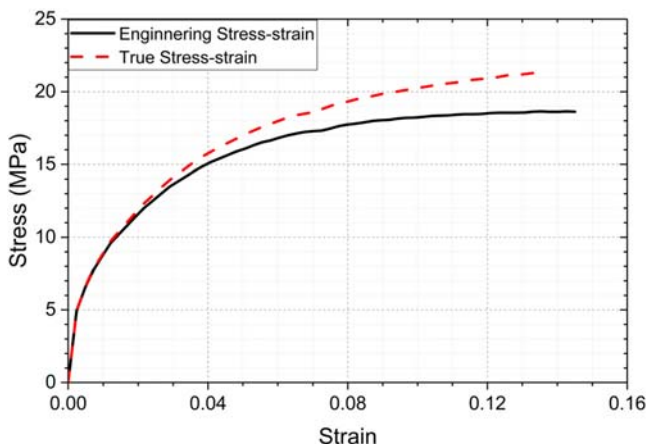
Figure 3. Stress-strain curves from tensile test.

Table 1. Material properties of the testing specimens.

Materials	Young's modulus E (MPa)	Poisson's Ratio ν
Fibreglass	45100	0.3
HDPE	961	0.4
UHMWPE	1080	0.4

of metallic flexible pipe. After that, Lu et al. (2010) used the same experimental method to get the bending stiffness of steel wires reinforced flexible pipeline. However, the test section is not under pure bending load in the three-point bending test, as there is a stress concentration on the test section. To avoid this flaw, Bai et al. (2015) investigated the bending behaviour of reinforced thermoplastic pipe (RTP) by using a four-point bending test, and the results of experiment and numerical simulation fit each other very well. Hence, the bending moment-curvature relationship of the FGRFP in this paper is also obtained by the four-point bending test.

2.3. Experimental facility

A typical four-point bending test is carried out on an experimental facility, whose diagrammatic sketch is shown in Figure 5. The dimensions of the experimental facility are shown in Table 2. As shown in Figure 4, the four-point bending test is carried out in the horizontal plane to eliminate the influence of the weight of the specimen. A loading beam pushed by a jack moves on the slider. The displacement of the beam is recorded by a displacement gauge. The load generated by the jack is recorded by a force sensor. According to the load and the displacement recorded by the force sensor and the displacement gauge, a moment-curvature relationship can be figured out.

The straight specimen, initially, is in the horizontal position, which is indicated by the solid line in Figure 5. After that, the loading beam and the loading roller move downwards together to exert a bending moment on the specimen. Consequently, the specimen, indicated by the dash line in Figure 5, tends to be bent and the rigid region of it begins to rotate an angle of α.

2.4. Specimen

The FGRFP specimen is formed by an inner UHMWPE layer, an outer HDPE layer and eight reinforced layers. HDPE (matrix) and fibreglass (embedded in the matrix) constitute the eight reinforced layers in which the winding angle of fibreglass in odd layers is +54.7°, while that in even layers is −54.7° (the opposite direction against +54.7°). It should be noted that the fibre volume ratio is

Table 2. Dimensions of the test facility.

Symbol	Value (mm)	Note
L	600	Length of the test section
L_1	800	Distance between loading points
L_2	1400	Distance between support points
l	300	Horizontal distance between loading point and support point

Figure 4. The four-point facility.

Table 3. Geometric parameters of testing specimens.

Parameter	Value
Inner radius (mm)	25
Outer radius (mm)	38
Thickness of inner PE layer (mm)	4
Thickness of outer PE layer (mm)	3
Number of reinforced layers	8
Winding angle of the fibreglass (°)	±54.7
Thickness of reinforced layers (mm)	6

Table 4. Valid length and diameter of specimens.

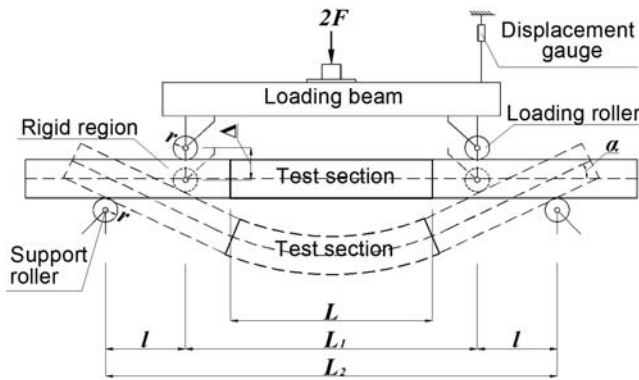| Specimen	Outer Diameter (mm)	Wall thickness (mm)	Initial ovalization (%)
#1	76.44	12.96	0.51
#2	76.58	13.35	0.10
#3	76.71	12.90	0.36

Figure 5. Diagrammatic sketch of facility.

50%. The nominal manufacturer dimensions of the specimens are shown in Table 3.

2.5. Experiment process

The thickness, outer diameter and length of the test specimens were measured before the test. The detailed valid dimensions of three specimens are shown in Appendix (Tables A1–A3). The general measured dimensions of the specimens are shown in Table 4.

The relative standard deviation (RSD) between the maximum and the minimum diameter is 0.17%, while the average of the outer diameter is 0.38% deviated from the nominal manufacturer size. It also can be found that the deviation of the measured thickness is 1.53%, which is also within the error limit. It presents that the experiment results of them are comparable. Furthermore, initial ovality of the specimens is all pretty small and no bigger than 1%. Thus, it can be concluded that the initial imperfection of the three specimens is quite small.

As shown in Figure 6. During the test, the loading beam was pushed by a jack, generating an increasing thrust (2F), and it slid forward at a constant speed. The displacement of the loading beam was recorded as Δ by the displacement gauge. When the loading beam was sliding forward, the FGRFP tended to bend under the bending moment generated by the four rollers.

The rigid region was formed by inserting a cylindrical rigid rod into the specimen. It should be noted that the length of the rigid rod is around 600 mm, which means that the length of rigid region is also around 600 mm. According to the loading condition of the specimens, the test section can be regarded as a pure bending region. In order to make sure that the pipe is subjected to a static load, the loading process must be slow, stable and constant by keeping the speed of the loading beam at about 0.2~0.4 mm/s. After the test, the displacement of the loading beam (Δ) and the load (2F) was converted into the curvature κ and the moment M from the following expression:

$$\Delta - [l \cdot \tan \alpha + (2r + D_0) - \frac{2r + D_0}{\cos \alpha}] = 0 \qquad (1)$$

$$\kappa = \frac{2\alpha}{L} \qquad (2)$$

$$M = \frac{F}{\cos \alpha} \cdot [\frac{l}{\cos \alpha} - (2r + D_0) tan \, \alpha] \qquad (3)$$

Where α is the inclination angle of the rigid region with respect to the horizontal line, r is the diameter of the roller, D_0 is the outer diameter of the rigid region, l is the horizontal distance between the loading roller and the support roller, L is the length of the test section, and F is half the thrust generated by the jack.
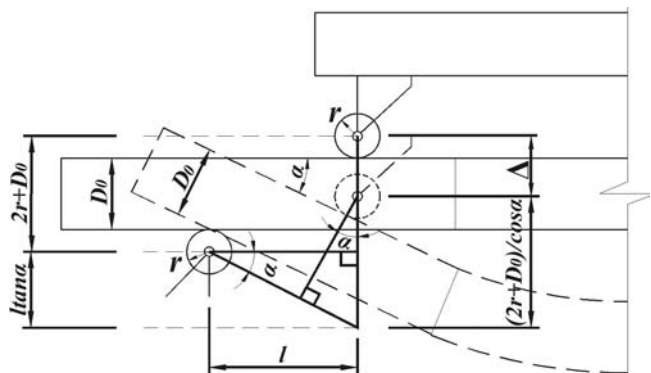

Figure 6. Geometric relationship between α and Δ.

According to the geometric relationship between α and Δ shown in Figure 6, Equation 1 can be obtained. Equation 3 are proved in Appendix (shown in Figures A1 and A2).

2.6. Experimental results

At the end of the test, the photographs of the samples were taken, and the curvature-moment relationships were obtained. From Figures 7(a–c), it can be observed that the samples bent excessively under bending load.

Figure 8 shows that the moment gradually rises as the curvature increases, and the three test curves are close to each other. Although the test curves have a slight fluctuation, they maintain a relatively steady rise. This means that the test result is reasonable. The summary of the bending test data is shown in Table 5.

3. Numerical simulation method (NSM)

In this part, a finite element model (FEM) is established to study the mechanical behaviour of the FGRFP by using the Abaqus™/Standard nonlinear finite element analysis tool. The geometrical dimensions of the FEM are consistent with those from manufacture.

3.1. Parts and properties

As shown in Figure 9, a 300 millimetres long numerical model (semi-structure) of the FGRFP consists of ten layers: an outer layer, an inner layer and eight reinforced layers. During the manufactory process, each layer of the pipe is bonded firmly. The reinforcement considered here is produced by the helical tape wrapping method, using prepreg tapes (shown in Figure 2) in which impregnated twisted glass fibres are embedded in the HDPE matrix. Since the twisted glass fibres are impregnated firmly, the reinforced layers are considered as an integral part. Considering how the pipes are made, extrusion and partition commands were used to separate the 300 millimetres long part into ten cells in its radial direction, and each one of them represents one layer. The inner and outer layers, which are made of ordinary HDPE and UHMWPE respectively, are isotropic, while the reinforced layers made of fibreglass reinforced HDPE are orthotropic. Therefore, the three principal orientations need to be assigned to the different reinforced layers by using the material orientation assignment technique.

As shown in Figure 10, the local material coordinate system of the reinforced layers is designated as (1,2,3), where 1 is the direction of the fibre, 2 is the direction perpendicular to the glass-fibre strand in the plane, and 3 is the normal direction in the cylindrical coordinate system. Before the orientation assignment, the coordinate axis 1, 2 and 3 are directed at the radial, hoop and axial direction respectively. It means the direction of the fibre is along the axial direction of the pipe. For instance, one reinforced layer of the model before the orientation is shown in Figure 10(a). Then the coordinate system (1,2,3) rotates about the axis 3 by an additional rotation (−54.7° for even reinforced layers or 54.7° for odd reinforced layers). As shown in Figure 10(b), the coordinate system (1,2,3) of the same reinforced layer is rotated by 54.7° after the orientation assignment.

(a) Specimen 1

(b) Specimen 2

(c) Specimen 3
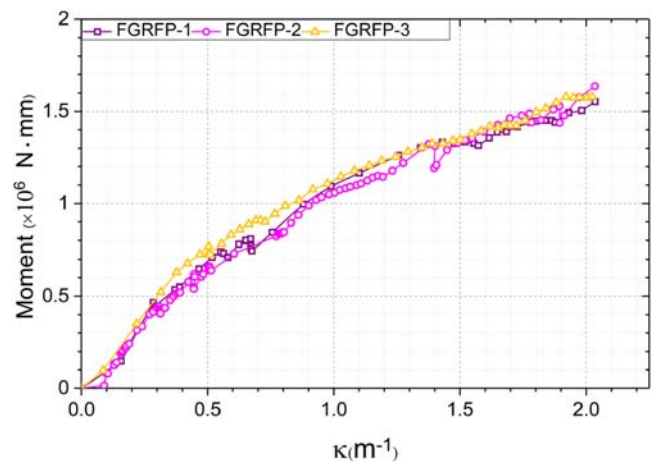
Figure 7. Bending deformation of the three specimens.

Figure 8. Curvature-moment curves of three test specimens.

Table 5. Summary of the bending test data.

| Specimen	Displacement (mm)	Curvature (m^{-1})	Moment ($\times 10^6$ N · mm)
FGRFP1	182.20	2.036	1.552
FGRFP2	182.12	2.035	1.637
FGRFP3	180.91	2.023	1.581

Figure 9. Break out the section of FEM.

3.2. Simplified model of reinforced layer

3.2.1. Simplification in linear elasticity stage

As described in the introduction part, the reinforced layer consists of HDPE matrix and fibreglass, hence the mechanical characteristics of fibreglass and HDPE matrix shown in Table 1 can be transformed into the nine local direction's elastic constants of each reinforced layer by using the simplification model of the reinforced layer. Then, nine elastic constants (E_1, E_2, E_3, G_{12}, G_{13}, G_{23}, ν_{12}, ν_{13}, ν_{23}) can be used to define the engineering elastic constants of the numerical model's reinforced layers in the Abaqus™.

In this part, the glass fibres, which are in each of the reinforced layers or prepreg tapes, are simplified as equidistant from each other. Hence, it can be considered that each of prepreg tapes consists of a large quantity of representative units as shown in Figure 11. The length of the representative unit is equal to the space between fibres. Then, according to the volume ratio of the glass-fibre in the prepreg tape, the space between fibres can be obtained. For a convenient calculation of the nine elastic constants of the reinforcement, the representative unit is taken as an equivalent unit. Compared to the representative unit, the equivalent unit have the same size and volume ratio of the glass-fibre, but, a different cross-section of the fibre (one is circular and another is a square).

As shown in Figure 11, a global cylindrical coordinate system is established. The coordinate axis r, θ and z denote the radial, hoop and axial direction respectively. The local material coordinate system of the reinforced layers is designated as (1,2,3), where 1 is the direction of the fibre, 2 is the direction perpendicular to the glass-fibre strand in the plane, and 3 is the normal direction in the cylindrical coordinate system. φ is the winding angle (54.7°) of fibres in reinforced layers. d_G is the diameter of glass-fibre, and h is the thickness of each reinforced layer or prepreg
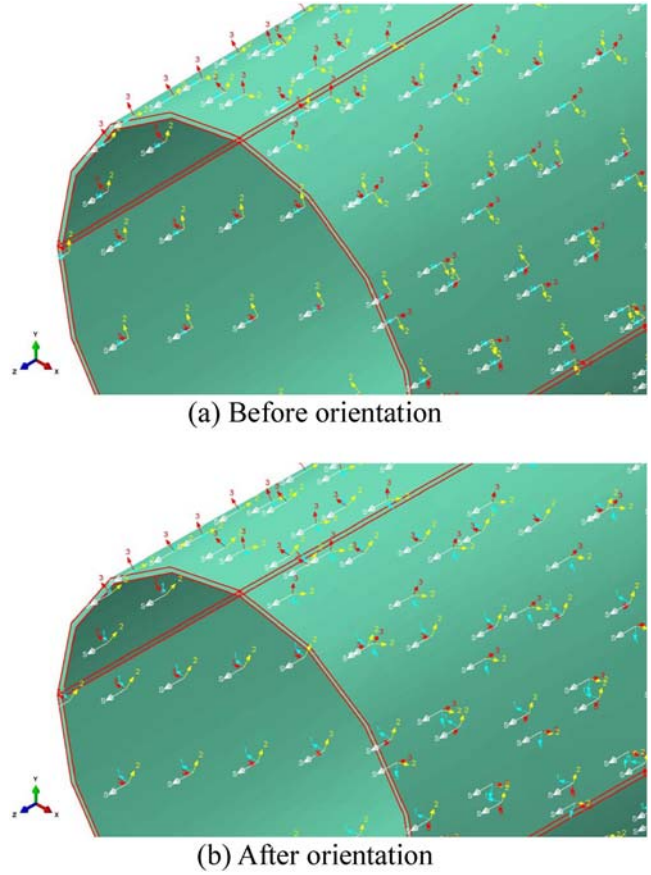
Figure 10. Discrete field of one layer before and after orientation.

tape. According to the dimension of prepreg tape provided by manufacturer, $d_G = h$. b is the space between fibres. This space can be calculated by following formula (Zhu 2007).

$$b = \frac{2\pi R_i}{2\pi R_i h V_{FB}/S_{FB}} = \frac{\pi h}{2} \approx 1.18\,\text{mm} \qquad (4)$$

Where R_i is diameter of i th reinforced layer; V_{FB} is the volume
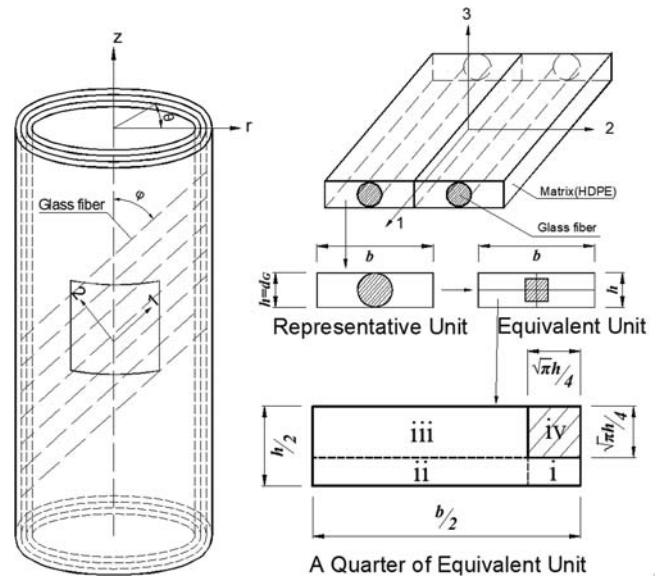
Figure 11. Simplification of the reinforced layer.

ratio of the glass-fibre $V_{FB} = 50\%$; S_{FB} is the cross-section area of glass-fibre $S_{FB} = \dfrac{\pi h^2}{4}$.

As shown in Figure 11, the cross-section of fibre is a square in the equivalent unit, while the actual shape is circular. In order to make sure that the volume ratio of the matrix and fibre is not changed after the simplification, the area of the square in the equivalent unit should be equal to the actual area of the cross-section of the fibre, which is S_{FB}. Therefore, the length of each side of the square in the equivalent unit is $\sqrt{S_{FB}} = \dfrac{\sqrt{\pi}h}{2}$.

Based on simplification of reinforced layer shown in Figure 11, nine elastic constants of the reinforced layers $E_1, E_2, E_3, G_{12}, G_{13}, G_{23}, \nu_{12}, \nu_{13}, \nu_{23}$ can be determined (Zhu 2007).

$$E_1 = E_{FB}V_{FB} + E_{PE}V_{PE} \tag{5}$$

$$E_2 = \frac{E_{FB}E_{PE}V_I}{E_{PE}\dfrac{V_{FB}}{V_I} + E_{FB}(1 - \dfrac{V_{FB}}{V_I})} + E_{PE}(1 - V_I) \tag{6}$$

$$E_3 = \frac{E_{FB}E_{PE}\dfrac{V_{FB}}{V_I}}{E_{PE}V_I + E_{FB}(1 - V_I)} + E_{PE}(1 - \dfrac{V_{FB}}{V_I}) \tag{7}$$

$$G_{12} = G_{13} = \frac{G_{FB}G_{PE}\dfrac{V_{FB}}{V_I}}{G_{PE}V_I + G_{FB}(1 - V_I)} + G_{PE}(1 - \dfrac{V_{FB}}{V_I}) \tag{8}$$

$$G_{23} = \frac{G_{FB}G_{PE}V_I}{G_{PE}\dfrac{V_{FB}}{V_I} + G_{FB}(1 - \dfrac{V_{FB}}{V_I})} + G_{PE}(1 - V_I) \tag{9}$$

$$\nu_{12} = \nu_{13} = \nu_{FB}V_{FB} + \nu_{PE}(1 - V_{FB}) \tag{10}$$

$$\nu_{23} = \frac{\nu_{FB}V_{FB} + \nu_{PE}\dfrac{E_{FB}}{E_{PE}}(V_I - V_{FB})}{\dfrac{V_{FB}}{V_I} + \dfrac{E_{FB}}{E_{PE}}(1 - \dfrac{V_{FB}}{V_I})} + \nu_{PE}(1 - V_I) \tag{11}$$

Where E_{PE}, ν_{PE}, G_{PE} is Young's modulus, Poisson's ratio and shear modulus of the HDPE matrix, E_{FB}, ν_{FB}, G_{FB} is Young's modulus, Poisson's ratio and shear modulus of the fibre-glass, V_{PE}, V_{FB} is the volume ratio of the matrix and fibre. V_I is the volume ratio of area iii and area iv, as shown in Figure 11. V_I can be obtained by:

$$V_I = \frac{\sqrt{\pi}h/4}{h/2} = \frac{\sqrt{\pi}}{2} \tag{12}$$

In specific, the volume ratio of the representative or equivalent unit equals one. Therefore, $V_{PE} = 1 - V_{FB}$.

The calculation result of the reinforced layer's elastic constants is used to define the engineering elastic constants of the numerical model's reinforced layers in the Abaqus™.

The calculation result of the reinforced layer's elastic constants is shown in Table 6.

3.2.2. Simplification in elastic-plastic stage

In this part, the reinforced layer's true stress–strain curves of three global cylindrical directions (r, θ, z) can be calculated

Table 6. Elastic constants of reinforced layer.

Elastic constants	Value
E_1	23151.80 MPa
E_2	2502.73 MPa
E_3	5465.85 MPa
G_{12}	1971.57 MPa
G_{13}	1971.57 MPa
G_{23}	896.00 MPa
ν_{12}	0.35
ν_{13}	0.35
ν_{23}	0.40

by using Equations 4–17. For a convenient formulation, vector C_i in this section represents any of the nine engineering constants vector $E_1, E_2, E_3, G_{12}, G_{13}, G_{23}, \nu_{12}, \nu_{13}, \nu_{23}$. Firstly, the tangent modulus vector E_{PE} of the HDPE can be transformed into C_i. Then, nine vectors C_i are transformed into three reinforced layer's modulus vectors E_z, E_r, E_θ. In the end, the reinforced layer's true stress–strain curves of three global cylindrical directions (r, θ, z) can be calculated by using the numerical integration method. All this procedure is constructed in the Matlab™. The detailed equations of C_i, $E_1, E_2, E_3, G_{12}, G_{13}, G_{23}, \nu_{12}, \nu_{13}, \nu_{23}, E_z, E_r, E_\theta, E_{PE}$ are illustrated in Appendix (Equations A1–A14).

By employing first-order interpolation in the Matlab™, a set of stress–strain discrete data point is obtained based on the stress–strain curve of HDPE (shown in Figure 3). Every data point can be used to calculate a corresponding secant modulus E_{PE}^k by using numerical differentiation method as shown in Equation 13. It should be noted that when the number of data points is large enough, the secant modulus E_{PE}^k approaches to the tangent modulus of the corresponding data point.

$$E_{PE}^k = \frac{\sigma_{PE}^{k+1} - \sigma_{PE}^k}{\varepsilon_{PE}^{k+1} - \varepsilon_{PE}^k}, (k = 1, 2 \ldots, n) \tag{13}$$

Where σ_{PE}^k is the HDPE's true stress of the kth data point; ε_{PE}^k is the HDPE's true strain of the kth data point n is the number of data points.

Then, the E_{PE} of the HDPE can be obtained. By substituting E_{PE} into Equations 5–11, the nine vectors C_i are constructed.

In the local cylindrical coordinate system, the flexibility matrix of each reinforced layer can be expressed as (Zhu 2007):

$$S^k = \begin{pmatrix} \dfrac{1}{E_1^k} & -\dfrac{\nu_{12}^k}{E_2^k} & -\dfrac{\nu_{13}^k}{E_3^k} & 0 & 0 & 0 \\ -\dfrac{\nu_{12}^k}{E_1^k} & \dfrac{1}{E_2^k} & -\dfrac{\nu_{23}^k}{E_3^k} & 0 & 0 & 0 \\ -\dfrac{\nu_{13}^k}{E_1^k} & -\dfrac{\nu_{23}^k}{E_2^k} & \dfrac{1}{E_3^k} & 0 & 0 & 0 \\ 0 & 0 & 0 & \dfrac{1}{G_{23}^k} & 0 & 0 \\ 0 & 0 & 0 & 0 & \dfrac{1}{G_{13}^k} & 0 \\ 0 & 0 & 0 & 0 & 0 & \dfrac{1}{G_{12}^k} \end{pmatrix}^k \tag{14}$$

In the global cylindrical coordinate system, the flexibility

matrix of each reinforced layer can be expressed as:

$$\bar{S}^k = TS^kT^T \tag{15}$$

Where:

$$T = \begin{pmatrix} \cos^2\varphi & \sin^2\varphi & 0 & 0 & 0 & \cos\varphi\sin\varphi \\ \sin^2\varphi & \cos^2\varphi & 0 & 0 & 0 & -\cos\varphi\sin\varphi \\ 0 & 0 & 1 & 0 & 0 & 0 \\ 0 & 0 & 0 & \cos\varphi & \sin\varphi & 0 \\ 0 & 0 & 0 & -\sin\varphi & \cos\varphi & 0 \\ -2\cos\varphi\sin\varphi & 2\cos\varphi\sin\varphi & 0 & 0 & 0 & \cos^2\varphi-\sin^2\varphi \end{pmatrix} \tag{16}$$

$$\bar{S}^k = \begin{pmatrix} \dfrac{1}{E_z^k} & -\dfrac{v_{rz}^k}{E_r^k} & -\dfrac{v_{\theta z}^k}{E_\theta^k} & 0 & 0 & 0 \\ -\dfrac{v_{zr}^k}{E_z^k} & \dfrac{1}{E_r^k} & -\dfrac{v_{\theta r}^k}{E_\theta^k} & 0 & 0 & 0 \\ -\dfrac{v_{z\theta}^k}{E_z^k} & -\dfrac{v_{r\theta}^k}{E_r^k} & \dfrac{1}{E_\theta^k} & 0 & 0 & 0 \\ 0 & 0 & 0 & \dfrac{1}{G_{r\theta}^k} & 0 & 0 \\ 0 & 0 & 0 & 0 & \dfrac{1}{G_{z\theta}^k} & 0 \\ 0 & 0 & 0 & 0 & 0 & \dfrac{1}{G_{zr}^k} \end{pmatrix}^k \tag{17}$$

Where $k = 1, 2 \ldots., n$.

After that, the nine vectors C_i are substituted into Equation 15, and the global modulus vectors E_z, E_r, E_θ of reinforced layers shown in Figure 12 is obtained by solving those equation.

Finally, the reinforced layer's true stress–strain discrete curves of the three directions (r, θ, z) can be calculated based on the global modulus vectors E_z, E_r, E_θ of reinforced layers by using the numerical integration method in the Matlab™. The three true stress–strain curves of the reinforced layer are shown in Figure 13.

According to the knowledge of material mechanics, the axial stress is a type of primary stress compared with the radial and the circumferential stress when the pipe is under pure bending. When the radial stress and the circumferential stress are small, the stress–strain curve is approximately linear, as shown in Figure 13. Additionally, the results of the numerical simulation show that the circumferential and the radial deformation are pretty small compared to the axial deformation. Furthermore, the stress–strain curve in axial direction represents the effect of stress–strain curve in direction (1,2,3) to direction z. Hence, the stress–strain curve in the circumferential and the radial direction can be regarded as approximately linear, and only the stress–strain in direction z is used to define the yield stress-plastic strain curve of the reinforced layers in NSM. This is also the reason why STM only considers the axial tangent module's (E_z) contribution to the ultimate bending moment (stated in the Section 4.1).
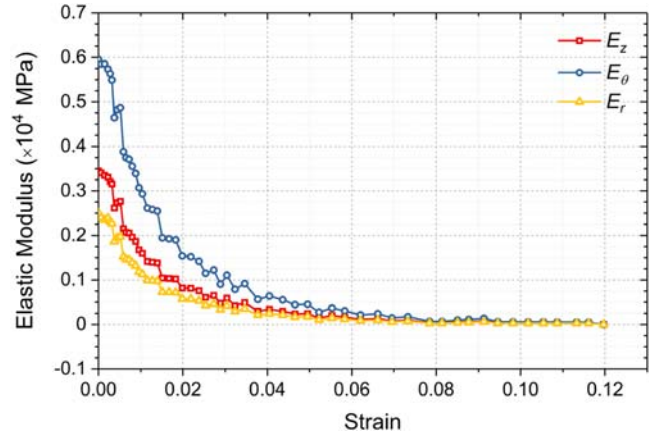

Figure 12. Reinforced layer's modulus (E_z, E_r, E_θ)-strain curves in three global directions.

The true stress–strain curve of the reinforced layer in the axial direction (direction z) is used to define the yield stress-plastic strain curve of FEM's reinforced layers and also used to calculate the stress of axial direction in STM.

3.3. Boundary conditions and Mesh

As shown in Figure 14, symmetric boundary condition about the axial direction (z axis) is applied to the right side of the pipe (U3 = UR1 = UR2 = 0) and a kinematic coupling constraint is established at the other end. This type of constraint can apply a uniform rotation on the left side and freely allow the ovalization deformation on the right side. The bending process is achieved by applying a rotation about the x-axis at the reference point of the coupling, and the nonlinear static analysis including non-linear geometric effects is selected for large displacement effects.

3D solid element (C3D8I) is selected for the inner layers, the outer layers and the reinforced layers. This type of element is more effective to provide relatively high accuracy than second-order elements. As shown in Figure 15, the whole model contains 39000 elements and 43472 nodes. The global size of the elements is 4 mm.
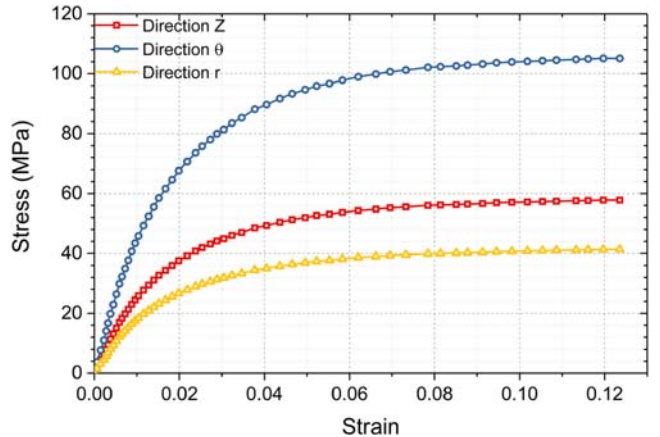

Figure 13. Reinforced layer's true stress-strain curves in three global directions.
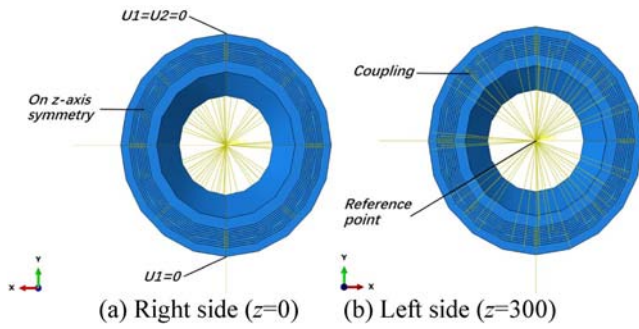
Figure 14. Boundary condition of the FEM model.

4. Simplified theoretical method (STM)

4.1. Assumptions of STM

Based on the actual stress characteristics of the samples, the following assumptions are proposed to focus on the bending problem with the engineering applications point of view.

(a) The FGRFP consists of the outer layers, inner layers and reinforced layers, and each reinforced layer consists of the HDPE matrix and filament glass fibres.
(b) The materials including HDPE and filament glass fibres are continuous, homogeneous and flawless.
(c) The inner and outer layers are isotropic, and the reinforced layers are orthotropic.
(d) STM only considers the axial tangent module's (E_z) contribution to the ultimate bending moment of the FGRFP
(e) STM doesn't take the deformation in the cross section of the pipe into consideration.
(f) The neutral surface does not move during the bending process

4.2. Definition of STM

A long, circular pipe with radius R and wall thickness t loaded by a pure bending load is shown in Figures 16 and 17. The curvature and deformation of the cross section are uniform along the length of the pipe under the pure bending load.
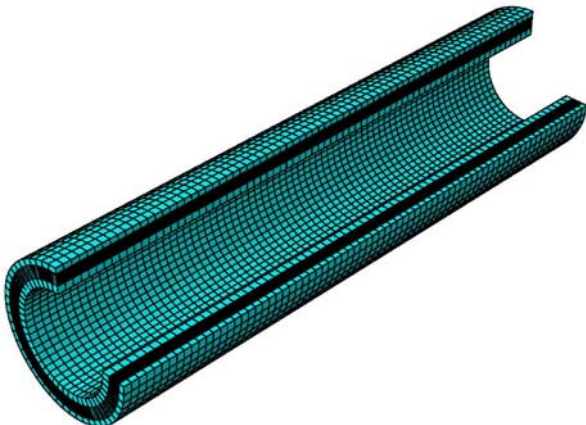
According to the Euler–Bernoulli beam theory neglecting the deformation of cross-section, the axial strain is given:

$$\varepsilon_z(r, \theta, \kappa) = \xi(r, \theta)\kappa \tag{18}$$

where:

$$\xi(r, \theta) = r \cos \theta \tag{19}$$

θ, r–the coordinates of the integral point in polar coordinates; κ–the curvature of the 600 mm pipe; ξ–the perpendicular distance from the integral point to the neutral surface of the pipe.

Then, the stress ($\sigma_z(r, \theta, \kappa)$) in the axial direction can be obtained based on the stress–strain curve in the axial direction (Figure 13) by the linear interpolation method in the Matlab^{TM}.

Finally, the moment under different curvature can be expressed as:

$$M(\kappa) = \int_0^{2\pi} \int_{R_i}^{R_o} \xi(r, \theta)\sigma_z(r, \theta, \kappa)drd\theta \tag{20}$$

Where R_o–the outer diameter of the pipe; R_i–the inner diameter of the pipe. In the STM calculation, the pipe cross section is discretized into N_r and N_θ elements along radial and circumferential directions, respectively. It mean the cross section of the pipe is divided into $N_r \times N_\theta$ elements totally. The centre point of each elements represents the coordinate of this element. According to the
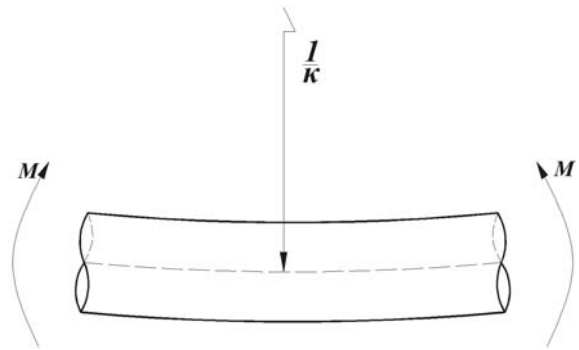

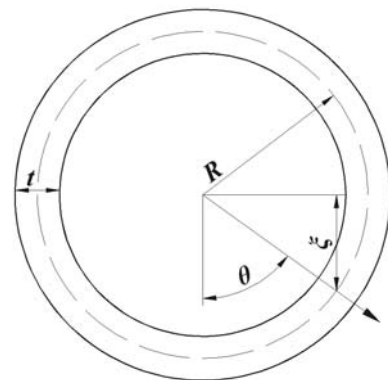**Figure 16.** Infinite long FGRFP under pure bending.

Figure 15. Break out the section of meshed model.

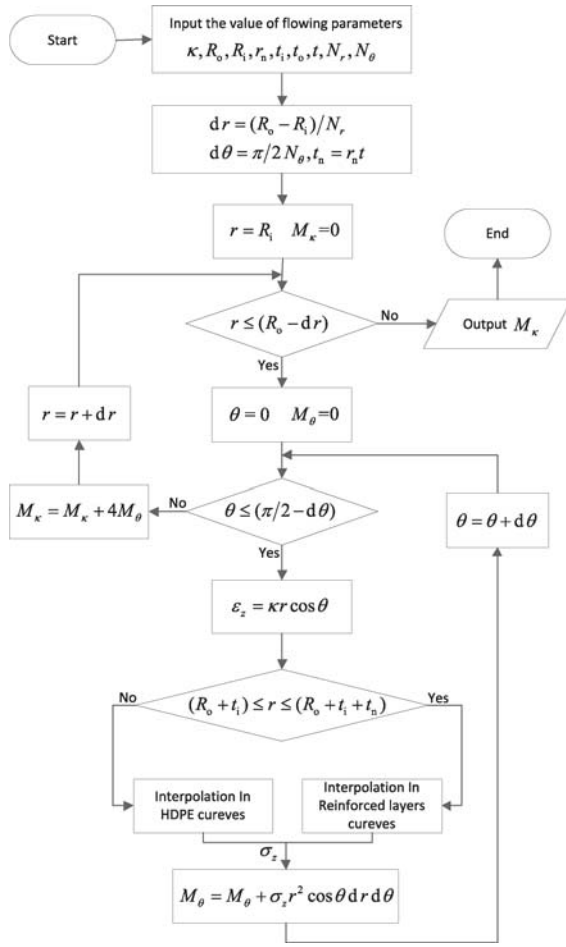**Figure 17.** Diagrammatic sketch of the cross section.

Figure 18. Algorithms of STM.

coordinate (θ, r), the axial strain can be calculated by Equation 18. Then, linear interpolation is used to calculate the corresponding axial stress in Matlab^{TM}.

The specific algorithm is shown in Figure 18:

Where t_i– the thickness of the inner layer; t_o– the thickness of the outer layer; t– the thickness of one reinforced layer; r_n– the number of the reinforced layer; t_n– the thickness of the reinforced layer; N_r– the number of the radial integral element; N_θ– the number of the circular integral element.

4.3. Results of experiment, STM and NSM

The curvature-moment curves of the experiment, STM and NSM are shown in Figure 19. This curve shows nonlinearity with the increasing bending moment, which is due to the nonlinearities of material and deformation of cross section. Due to the displacement limit of the loading beam (mainly because of the displacement limit of the jack), the three test curves don't show their ultimate bending moment. Nevertheless, the experiment curve shows almost the same uptrend with the numerical simulation result. Compared to the NSM, the curve of STM fails to decline when the curvature is larger than 3.55 m^{-1}. The reason for this phenomenon is mainly that STM does not take into consideration the deformation in cross section of the

pipe. It means that the cross section of the model in STM remains the same shape instead of becoming ovalization. By comparison, the cross section of FEM can become ovalization which causes a decline in the section stiffness of the model. This is also the reason that the curve of STM is a little bit higher than NSM in the up stage. However, the uptrend of the curve obtained by STM still agrees with both NSM and experiment. In general, results from NSM, STM and experiment show consistence with each other. Furthermore, the ultimate moment and curvature obtained from NSM, which are 1.79×10^6N·mm and 3.55 m^{-1}, are marked with a black pentagram in Figure 19. The ultimate moment obtained from STM is very close to the one collected from NSM, which are 1.80×10^6N·mm and 1.79×10^6N·mm respectively, and the RSD between them is 0.43%. In conclusion, it is safe to say that STM and NSM all achieve their expected goals.

5. Parametric study

In this section, the effects of several important parameters are investigated based on STM and NSM. Those parameters' influences on the ultimate curvature and moment, the deformation development of the cross-section and the comparison between the two methods (STM and NSM) is involved into discussion. It should be noted that the legends of the figures in this section follow a fixed format. For instance, one of the legends in Figure 22 is 'D_130_t_13 _D/t_10_A_30'. 'D_130' means the outer diameter of the model is 130 mm. 't_13' means the wall thickens of the model is 13 mm. 'D/t_10' means the diameter-thickness ratio of the model is 10. 'A_30' means the winding angle of the fibres is 30 degrees.

As the NSM takes the deformation of cross-section into consideration, every moment-curvature curve obtained by NSM has a peak point due to both the non-linear of material and the ovalization deformation of the cross-section. Then, the moment value will drop down after this point. Hence, the moment and curvature of the peak point can be regarded as the ultimate moment and ultimate curvature respectively. However, the moment-curvature curves calculated by STM don't have a peak point, for this method doesn't consider the deformation in the cross-section. In spite of it, the curve of STM also can reach horizontal due to the non-linear of material (as shown in Figure 13). Therefore, the moment on the horizontal line can be considered as the ultimate moment.

5.1. Deformation of cross-section

The deformation development of the cross-section is presented in the ovality-curvature curves (Figures 20–22). The ovality corresponding to the ultimate curvature is marked with a pentagram on the curves. This ovality can be expressed as Ovality$_U$.

The ovality of the pipe can be calculated by:

$$\text{Ovality} = \frac{D_{\max} - D_{\min}}{D_{\text{initial}}} \times 100\% \qquad (21)$$
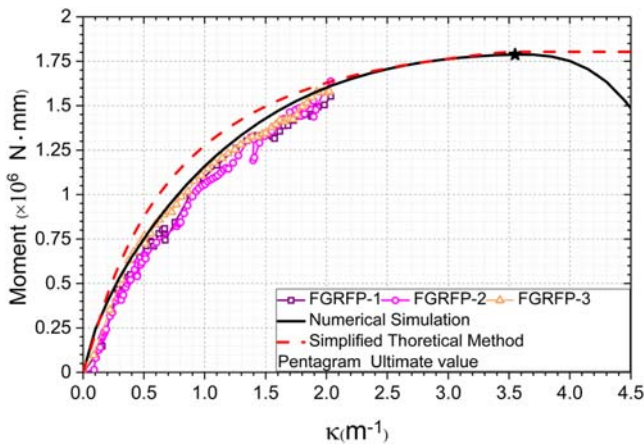
Figure 19. Comparison of results from experiment, STM and NSM.

Figure 21. Ovality-curvature curves of NSM with a constant D/t ratio.

Where D_{max}–the maximum outer diameter of the pipe; D_{min}–the minimum outer diameter of the pipe; $D_{initial}$–the initial outer diameter of the pipe.

5.1.1. Different outer diameters

Eight cases have the same wall thickness (13 mm) and winding angle (54.7 degrees), but different outer diameters, as shown in Figure 20. Furthermore, the pipe wall consists of a 4 mm inner layer, 3 mm outer layer and 6 mm reinforced layer.

Obviously, the pipe with a larger outer diameter has larger ovalization deformation in the cross section when the curvature is the same. For all curves, the ovality increases as the curvature gets larger, but at different rates. In other words, the cross section of the pipe with a bigger outer diameter deforms more easily.

From the pentagrams on Figure 20, it can be observed that the bigger the diameter-thickness ratio of the pipe is, the larger the $Ovality_U$ is. The detailed data in Table 7 proves this conclusion. The mean value of the last column is 16.88%, meanwhile, the RSD of them is 34%. The value of the RSD proves that the $Ovality_U$ and the diameter-thickness ratio do have a clear correlation with each other. More specifically, there is a positive relationship between them.
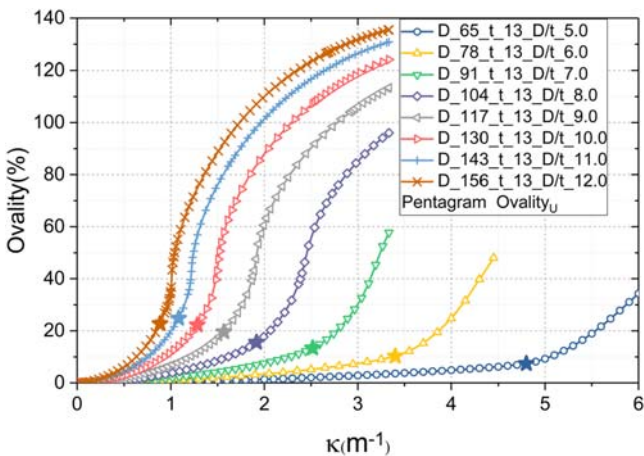
5.1.2. A constant diameter-thickness ratio

As shown in Figure 21, eight cases have the same diameter-thickness ratio ($D/t = 5.8$). The winding angle of the cases is 54.7 degrees. In addition, it should be noted that the wall thickness is changed just by adjusting the number of the reinforced layers and the wall thickness of the inner and outer layer (4 and 3 mm separately) does not change.

Different from Figure 20, although each group in Figure 21 has the same diameter-thickness ratio, the pipe with a larger outer diameter becomes oval at a larger rate. It means that the cross section of the pipe deforms more easily when the wall thickness and outer diameter get larger in the same ratio.

As shown in Figure 21, it seems like that the pentagrams on these curves are on the same horizontal line. It means that the $Ovality_U$ of each pipe doesn't change evidently compared to Figure 20. The concrete data in Table 8 is consistent with it. Calculated based on the detailed number of this table, the mean value and the RSD of the last column are 9.90% and 3% separately. It presents that the $Ovality_U$ are nearly unchanging when the diameter-thickness ratio is a constant. It also means that there is a weak relationship between the outer diameter and the $Ovality_U$.

By comparing Table 8 with Table 7, it can be observed that the diameter-thickness ratio of Table 8 is between 5 and 6,

Figure 20. Ovality-curvature curves of NSM with different outer diameters.

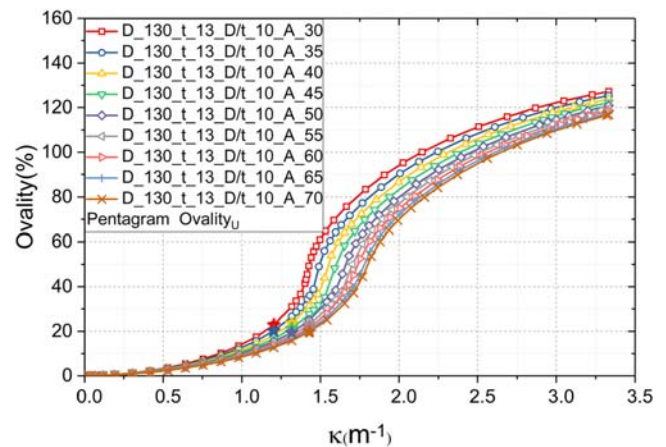**Figure 22.** Ovality-curvature curves of NSM with different winding angles.

Table 7. Ovality$_U$ of the pipes with different outer diameters.

D(mm)	t(mm)	D/t	Ovality$_U$ (%)
65	13	5	7.43
78	13	6	10.25
91	13	7	13.39
104	13	8	15.58
117	13	9	19.59
130	13	10	22.24
143	13	11	23.80
156	13	12	22.73

Table 9. Ovality$_U$ of the pipes with different winding angles

D(mm)	t(mm)	Winding angle (°)	Ovality$_U$ (%)
130	13	30	21.91
130	13	35	20.25
130	13	40	22.55
130	13	45	21.23
130	13	50	20.49
130	13	55	22.15
130	13	60	21.69
130	13	65	20.60
130	13	70	20.80

correspondingly, the mean value of the last column in Table 8 is between 7.43% and 10.25%. It accords with the positive correlation between the Ovality$_U$ and the diameter-thickness ratio.

5.1.3. Different winding angles

As shown in Figure 22, those nine cases have the same outer diameter (130 mm) and wall thickness (13 mm), but with different winding angles of the fibres in the reinforced layers.

It can be observed that the shape of these curves is similar to each other. The deformation rate of pipe with different winding angle differs from each other. Specifically, the pipe with a smaller winding angle deforms at a higher rate. It means that the cross section of the pipe deforms more easily when the winding angle is smaller. However, compared to Figures 20 and 21, the influencing of the winding angle on the deformation development of the cross section is smaller than the outer diameter.

As shown in Figure 22, it can be observed that the pentagrams are concentrated in an area on the figure. It means that the Ovality$_U$ of each pipe doesn't change evidently compared to Figure 20. The data in Table 9 proves it. Calculated based on the concrete numbers of the table, the mean value and the RSD of the last column are 21.30% and 4% separately. It means that the Ovality$_U$ are nearly unchanging when the diameter-thickness ratio is a constant. It also means that there is a weak relationship between the winding angle and the Ovality$_U$.

5.1.4. Simple formula of Ovality$_U$

Based on the parametric study from Section 5.1 (a)–(c), it can conclude that the diameter-thickness ratio is the main parameter in influencing on the Ovality$_U$. More specifically, they have a linear correlation with each other, as shown in Figure 23.

Table 8. Ovality$_U$ of the pipes with a constant D/t ratio.

D(mm)	t(mm)	D/t	Ovality$_U$ (%)
49.3	8.5	5.8	9.50
58.0	10.0	5.8	10.01
66.7	11.5	5.8	9.88
75.4	13.0	5.8	9.62
84.1	14.5	5.8	10.29
92.8	16.0	5.8	10.21
101.5	17.5	5.8	10.13
110.2	19.0	5.8	9.54

By linear fitting in Matlab^{TM}, the relationship between them can be expressed as:

$$\text{Ovality}_U = 2.45 \times \frac{D}{t} - 3.91 \qquad (22)$$

Where D is the outer diameter of the pipe; t is the wall thickness of the pipe.

The R-Square of the result is 0.95. It proves that the linear correlation between the Ovality$_U$ and diameter-thickness ratio exists and Equation 22 obtained by the linear fitting method is reasonable.

Finally, the ovality of the FGRFP can be obtained when the pipe is under the ultimate bending moment or curvature. In other words, the FGRFP very likely reaches its bending capacity (ultimate bending moment or curvature) when the ovality of the cross section is equal to the Ovality$_U$.

5.2. Comparison between STM and NSM

In this section, moment-curvature curves are obtained by both STM and NSM. κ_u^{NSM} is the ultimate curvature calculated by NSM.

The STM does not take into consideration the deformation in the cross section of the pipe, while, NSM dose. Hence, there will be a difference between them, as shown in Figures 24–29. Then, a factor is introduced to modify STM. The correction factor can be expressed as:

$$K_{M_u} = \frac{M_u^{NSM}}{M_u^{STM}} \qquad (23)$$
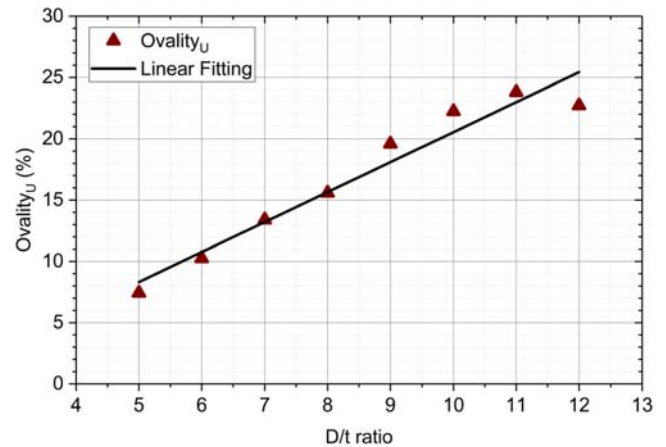
Figure 23. Linear fitting of Ovality$_U$-D/t ratio.

Where: M_u^{NSM} – Ultimate moment calculated by NSM; M_u^{STM} – Ultimate moment calculated by STM. Based on Equation 20, M_u^{STM} can be expressed as:

$$M_u^{STM} = \max(M(\kappa)) \qquad (24)$$

5.2.1. Different outer diameters

Eight cases have the same wall thickness (13 mm) and the different outer diameter, as shown in Figure 24. Furthermore, the pipe wall consists of a 4 mm inner layer, 3 mm outer layer and 6 mm reinforced layer. The winding angle of fibres in the reinforced layers is 54.7 degrees.

As shown in Figure 24, the dash line and solid line represent curves calculated by STM and NSM separately. The pentagram is the peak point of the curve. Every curve obtained by NSM has a peak point, then, they drop down after the peak point. Intuitively, it can be observed that the deviation between the two method increases as the outer diameter of the pipe gets larger.

As shown in Figure 25, the larger the outer diameter of the pipe is, the larger the ultimate moment is, meanwhile, the smaller the κ_u^{NSM} is. The M_u^{NSM} goes up from 1.26 kN · m to 7.42 kN · m as the outer diameter rises from 65 mm to 156 mm, while the M_u^{STM} goes up from 1.20 kN · m to 9.57 kN · m. Specifically, the ultimate moment increases by 6 times in NSM and 8 times in STM. Meanwhile, the κ_u^{NSM} decreases from 4.80 m^{-1} to 0.88 m^{-1} and decreases by 5.5 times. Hence, it can conclude that there will be a marked increase in bending capacity and decrease in bending flexibility when the outer diameter of the pipe gets larger.

More detailed data is shown in Table 10. The K_{M_u} decreases from 1.04 to 0.78 as the diameter-thickness ratio increases from 5 to 12. The RSD of the last column is 10%. It presents that there is a clear relationship between the K_{M_u} and the diameter-thickness ratio. More specifically, there is an anti-positive relationship between them.

5.2.2. A constant diameter-thickness ratio

As shown in Figure 26, eight cases have the same diameter-thickness ratio ($D/t = 5.8$), which is the same as the diameter-thickness ratio of the specimens. The winding angle of the cases is 54.7 degrees. In addition, it should be noted that the wall thickness is chang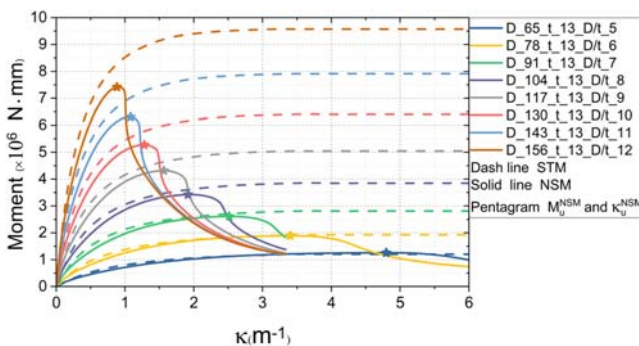ed just by adjusting the number of the reinforced layers. Instead, the wall thickness of the inner and outer layer (4 and 3 mm separately) doesn't change.

Similarly, the pentagram is the peak point of the curve. Every curve obtained by NSM has a peak point, then they drop down after the peak point, as shown in Figure 26.

As shown in Figure 27, along with the value of the outer diameter and wall thickness increasing, the ultimate moment of both methods increases, meanwhile, the κ_u^{NSM} decreases. The M_u^{NSM} goes up from 0.37 kN · m to 6.44 kN · m as the outer diameter rises from 49 mm to 110 mm, while the M_u^{STM} goes up from 0.36 kN · m to 6.88 kN · m. Specifically, the ultimate moment increases by 17 times in NSM and 19 times in STM. Meanwhile, the κ_u^{NSM} decreases from 6.10 m^{-1} to 2.39 m^{-1} and decreases by 2.5 times. It shows another conclusion that there will be a sharp increase in bending capacity and decrease in bending flexibility as the wall thickness and outer diameter get larger in the same ratio.

Concrete data in Table 11 presents that the K_{M_u} decreases from 1.03 to 0.94 as the outer diameter increases from 49 mm to 110 mm. The RSD of the last column is 3%. It means that the K_{M_u} is nearly unchanging when the diameter-thickness ratio is a constant.

5.2.3. Different winding angles

As shown in Figure 28, those nine cases have the same outer diameter (130 mm) and wall thickness (13 mm), but with different winding angles of the fibres in reinforced layers.

Similar to Figures 24, 26, and 28 also shows that every curve obtained by NSM has a peak point, then, they drop down after the peak point. It means that all the moment-curvature of the pipe has peak points and the curve will drop down after this point, no matter what the dimension parameters (outer diameter, wall thickness and winding angle) of the pipe are.

As shown in Figure 29, along with the value of the winding angle increasing, the ultimate moment of both methods decreases, meanwhile, the κ_u^{NSM} increases. The M_u^{NSM} goes down from 9.60 kN · m to 4.68 kN · m as the winding angle rises from 30 degrees to 70 degrees, while the M_u^{STM} goes down from 11.34 kN · m to 5.21 kN · m. Specifically, the ultimate moment decreases by 2 times in NSM and 2.17 times
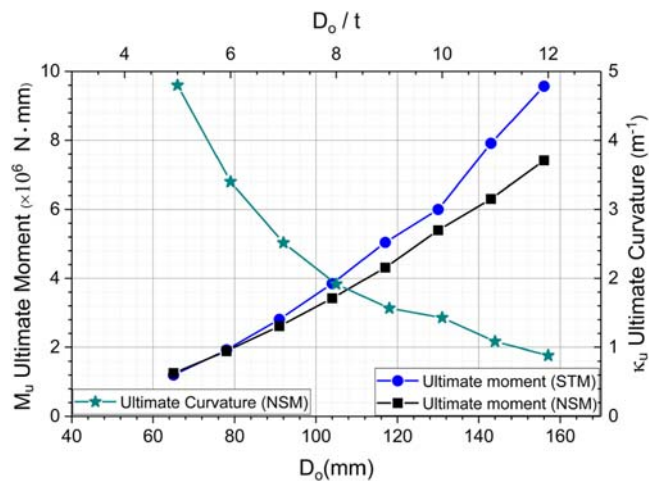

Figure 24. Moment-curvature curves of NSM and STM with different outer diameters.

Figure 25. The ultimate moment and curvature of the pipes with different outer diameters.
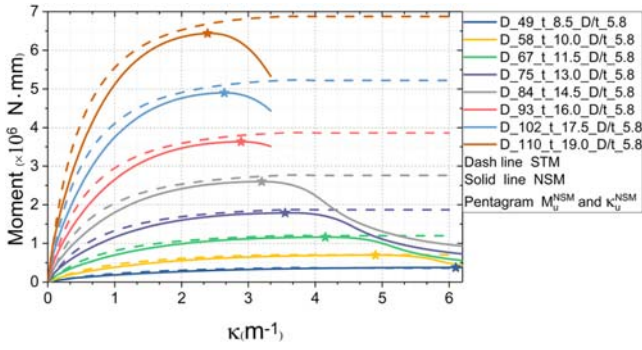
Figure 26. Moment-curvature curves of NSM and STM with a constant *D/t* ratio.

Figure 28. Moment-curvature curves of NSM and STM with different winding angles.

in STM. Meanwhile, the κ_u^{NSM} goes up from $1.20\,\mathrm{m}^{-1}$ to $1.43\,\mathrm{m}^{-1}$ and increases by 1.2 times. It presents that there will be a clear decrease in bending capacity and a small increase in bending flexibility as the winding angle increases.

Hence, compared to changing the winding angle, decreasing the outer diameter is a more efficient way to increase ultimate curvature.

Concrete data in Table 12 presents that the range of K_{M_u} increases from 0.83 to 0.90. The RSD of the last column is 3%. It means that the K_{M_u} is nearly unchanging when the winding angle changes.

5.2.4. Simple formula of K_{M_u}

Based on the parametric study from Section 5.2 (a)–(c), it can conclude that the diameter-thickness ratio is the main parameter in influencing on the K_{M_u}. More specifically, they have a linear correlation with each other, as shown in Figure 30.

By linear fitting in the Matlab™, the relationship can be expressed as:

$$\hat{K}_{M_u} = -0.04\frac{D}{t} + 1.21 \qquad (25)$$

Where $\hat{K}_{M_u}$ is the predicted value of K_{M_u}; D is the outer diameter of the pipe; t is the wall thickness of the pipe.

Figure 27. The ultimate moment and curvature of the pipes with a constant *D/t* ratio.

Figure 29. The ultimate moment and curvature of the pipes with different winding angles.

The R-Square of the result is 0.97. It proves that the linear correlation between the K_{M_u} and the diameter-thickness ratio exists and the Equation 25 obtained by the linear fitting method is reasonable.

Finally, the ultimate moment of the FGRFP can be calculated by using Equations 24 and 25.

$$M_u^{MSTM} = \hat{K}_{M_u} M_u^{STM} \qquad (26)$$

Where M_u^{MSTM} is the ultimate moment calculated by the modified STM.

As shown in Tables A4–A6, the differences of the ultimate moment between the modified STM and the NSM are pretty small. Hence, it is safe to say that the ultimate moment calculated by the modified STM are well consistent with the NSM.

Table 10. K_{M_u} of the pipes with different outer diameters.

D(mm)	t(mm)	D/t	M_u^{STM} ($\times 10^6$N · mm)	M_u^{NSM} ($\times 10^6$N · mm)	K_{M_u}
65	13	5	1.20	1.26	1.04
78	13	6	1.92	1.89	0.98
91	13	7	2.81	2.61	0.93
104	13	8	3.85	3.42	0.89
117	13	9	5.05	4.31	0.85
130	13	10	6.50	5.40	0.83
143	13	11	7.91	6.30	0.80
156	13	12	9.57	7.42	0.78

Table 11. K_{M_u} of the pipes with a constant D/t ratio.

D(mm)	t(mm)	D/t	M_u^{STM} ($\times 10^6$N $\cdot$ mm)	M_u^{NSM} ($\times 10^6$N $\cdot$ mm)	K_{M_u}
49.3	8.5	5.8	0.36	0.37	1.03
58.0	10.0	5.8	0.70	0.70	0.99
66.7	11.5	5.8	1.20	1.16	0.97
75.4	13.0	5.8	1.87	1.79	0.96
84.1	14.5	5.8	2.76	2.60	0.94
92.8	16.0	5.8	3.86	3.63	0.94
101.5	17.5	5.8	5.22	4.90	0.94
110.2	19.0	5.8	6.88	6.44	0.94

Table 12. K_{M_u} of the pipes with different winding angles.

D(mm)	t(mm)	Winding angle(°)	M_u^{STM} ($\times 10^6$N $\cdot$ mm)	M_u^{NSM} ($\times 10^6$N $\cdot$ mm)	K_{M_u}
130	13	30	11.34	9.60	0.85
130	13	35	9.36	8.14	0.87
130	13	40	8.03	7.12	0.89
130	13	45	7.11	6.37	0.89
130	13	50	6.46	5.81	0.90
130	13	55	6.50	5.40	0.83
130	13	60	5.65	5.09	0.90
130	13	65	5.40	4.86	0.90
130	13	70	5.21	4.68	0.90
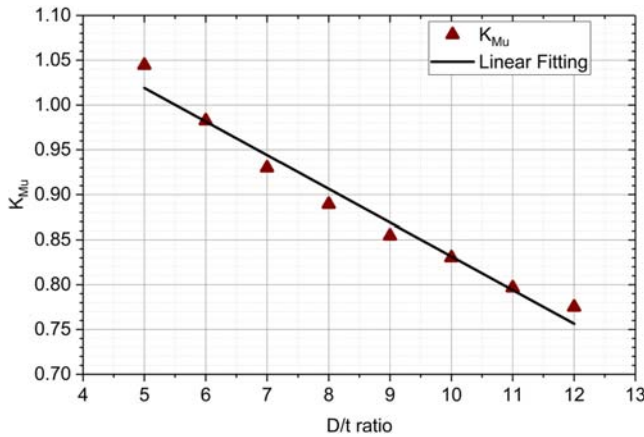
Figure 30. The linear fitting of K_{M_u}-D/t ratio.

5.2.5. Simple formula of ultimate curvature

As stated in Section 5.2 (a)–(c), both the outer diameter and the wall thickness have a clear influence on the ultimate curvature of the FGRFP, while, the influence of the winding angle on the ultimate curvature is pretty small. Accordingly, the outer diameter and the wall thickness are the key parameters in influencing on the ultimate curvature.

Then, based on data shown in in Tables A7 and A8 (including the ultimate curvature κ_u^{NSM}, the outer diameter D and the wall thickness t) a simple formula (Equation 27) of the ultimate curvature can be obtained by a surface fitting method. $\hat{\kappa}_u$ is the predicted ultimate curvature calculated by Equation 27.

$$\hat{\kappa}_u = \frac{1}{D(0.27D + 2.26) \cdot t^{-0.71}} \quad (27)$$

The R-Square of the surface fitting result is 0.99. It proves that Equation 27 obtained by the surface fitting method is reasonable.

The concrete data shown in Tables A7 and A8 indicates that the differences between κ_u^{NSM} and $\hat{\kappa}_u$ are pretty small. Therefore, it is safe to say that the predicted ultimate curvature $\hat{\kappa}_u$ calculated by Equation 27 are well consistent with the ultimate curvature obtained from the NSM.

6. Conclusions

In this paper, a simplified theoretical method (STM) is proposed to predict the ultimate moment of FGRFP under pure bending. Then the experimental method is used to prove the rationality of the numerical simulation method (NSM). After that, NSM is used as a benchmark to modify STM by introducing a factor. Furthermore, a simple formula used to calculate the factor is obtained by the linear fitting method. Finally, an extensive parametric study using both NSM and STM is carried out to analyze the influencing mechanisms on the deformation development of cross section, the ultimate moment and curvature of the FGRFP. Some conclusions can be drawn as follows:

(a) The results of the proposed NSM show great agreement with the experiment in the up stage of the curvature-moment curve. While the curves of the test fail to climb to the peak points due to the displacement limit of the loading beam.
(b) The Simple Formula of the correction factor obtained by the linear fitting method is reasonable. Meanwhile, the ultimate moment calculated by the modified STM is well consistent with the NSM.
(c) The Simple Formula of the ultimate curvature obtained by the surface fitting method is reasonable. Meanwhile, the ultimate curvature calculated by the Equation 27 is well consistent with the NSM.
(d) The diameter-thickness ratio is the main parameter in influencing on the Ovality$_U$. More specifically, they have a linear correlation with each other
(e) All three of the outer diameter, the wall thickness and the winding angle have a pretty clear influence on the ultimate moment of the FGRFP.
(f) Both the outer diameter and the wall thickness have an obvious influence on the ultimate curvature of the FGRFP, while the influence of the winding angle on the ultimate curvature is relatively small compared to the other two parameters.

The proposed methods and their results can not only provide references for the factory engineers during initial design and estimation, but also guide further investigation into other more complicated flexible pipes. Especially, the modified STM and the simple formula of the ultimate curvature provide a concise and relatively accurate way to predict the ultimate moment and curvature, which may be useful for engineering applications.

China to study the mechanical behaviour of FGRFP subjected to pure bending. The specimens used in the experiment are manufactured by Ningbo OPR Offshore Engineering Co. Ltd.

Disclosure statement

No potential conflict of interest was reported by the author(s).

References

Bai Y, Wang Y, Cheng P. 2013. Analysis of reinforced thermoplastic pipe (RTP) under axial loads. October 19-22, 2012. Proceedings of the ICPTT 2012: Better Pipeline Infrastructure for a Better Life. Wuhan, China.

Bai Y, Yu B, Cheng P, Wang N, Ruan W, Tang J, Babapour A. 2015. Bending behavior of reinforced thermoplastic pipe. J. Offshore Mech. Arct. Eng. 137(2): 021701.

Bodner S. 1987. Review of a unified elastic – viscoplastic theory. In: Miller AK, editor. Unified constitutive equations for creep and plasticity. Dordrecht: Springer; p. 273–301.

Colak OU, Dusunceli N. 2006. Modeling viscoelastic and viscoplastic behavior of high density polyethylene. Journal of Engineering Materials and Technology-transactions of The Asme - J ENG MATER TECHNOL. 128 (2006):572–578.

Dhar AS, Moore ID. 2006. Evaluation of local bending in profile-wall polyethylene pipes. J Transp Eng. 132:898–906.

Edmans BD, Pham DC, Zhang ZQ, Guo TF, Sridhar N, Stewart G. 2019. An effective multiscale methodology for the analysis of marine flexible risers. J Mar Sci Eng. 7:340.

Fang P, Xu Y, Yuan S, Bai Y, Cheng P. 2018. Investigation on mechanical properties of fibreglass reinforced flexible pipes under torsion. Proceedings of the ASME 2018 37th International conference on Ocean, offshore and arctic engineering; American Society of Mechanical Engineers Digital Collection.

Fredriksson DW, DeCew JC, Tsukrov I. 2007. Development of structural modeling techniques for evaluating HDPE plastic net pens used in marine aquaculture. Ocean Eng. 34:2124–2137.

Gibson A. 1989. Composite materials in the offshore industry. Met Mater. 5:590–594.

Hu H-T, Lin W-P, Tu F-T. 2015. Failure analysis of fiber-reinforced composite laminates subjected to biaxial loads. Composites Part B. 83:153–165.

ISO E. 2012. 527: 2012. Plastics-Determination of tensile properties.

Kagoura T, Ki I, Abe S, Inoue T, Hayashi T, Sakamoto T, Mochizuki T, Yamada T. 2003. Development of a flexible pipe for pipe-in-pipe technology. Furukawa Rev. 24:69–75.

Kruijer M, Warnet L, Akkerman R. 2005. Analysis of the mechanical properties of a reinforced thermoplastic pipe (RTP). Composites Part A. 36:291–300.

Li X, Zheng J, Shi F, Qin Y, Xu P. 2009. Buckling analysis of plastic pipe reinforced by cross-winding steel wire under bending. Proceedings of the ASME 2009 pressure vessels and piping conference; American Society of Mechanical Engineers Digital Collection.

Lu Q-z, Yue Q-j, Tang M-g, Zheng J-x, Yan J. 2010. Reinforced design of an unbonded flexible flowline for shallow water. Proceedings of the ASME 2010 29th International conference on ocean, offshore and Arctic engineering; American Society of Mechanical Engineers Digital Collection.

Menshykova M, Guz IA. 2014. Stress analysis of layered thick-walled composite pipes subjected to bending loading. Int J Mech Sci. 88:289–299.

Northcutt VM. 2000. Bonded flexible pipe. Proceedings of the OCEANS 2000 MTS/IEEE conference and exhibition conference proceedings (Cat No 00CH37158); IEEE.

Tonatto ML, Forte MM, Tita V, Amico SC. 2016. Progressive damage modeling of spiral and ring composite structures for offloading hoses. Mater Des. 108:374–382.

Tonatto ML, Tita V, Araujo RT, Forte MM, Amico SC. 2017. Parametric analysis of an offloading hose under internal pressure via computational modeling. Mar Struct. 51:174–187.

Tonatto ML, Tita V, Forte MM, Amico SC. 2018. Multi-scale analyses of a floating marine hose with hybrid polyaramid/polyamide reinforcement cords. Mar Struct. 60:279–292.

Troina L, Rosa L, Viero PF, Magluta C, Roitman N. 2003. An experimental investigation on the bending behaviour of flexible pipes. Proceedings of the ASME 2003 22nd International conference on offshore mechanics and arctic engineering; American Society of Mechanical Engineers Digital Collection.

Xia M, Kemmochi K, Takayanagi H. 2001. Analysis of filament-wound fiber-reinforced sandwich pipe under combined internal pressure and thermomechanical loading. Compos Struct. 51:273–283.

Xing J, Geng P, Yang T. 2015. Stress and deformation of multiple winding angle hybrid filament-wound thick cylinder under axial loading and internal and external pressure. Compos Struct. 131:868–877.

Xu Y, Bai Y, Fang P, Yuan S, Liu C. 2019. Structural analysis of fibreglass reinforced bonded flexible pipe subjected to tension. Ships Offsh Struct. 14:777–787.

Zhang C, Moore ID. 1997a. Nonlinear mechanical response of high density polyethylene. Part I: experimental investigation and model evaluation. Polym Eng Sci. 37:404–413.

Zhang C, Moore ID. 1997b. Nonlinear mechanical response of high density polyethylene. Part II: uniaxial constitutive modeling. Polym Eng Sci. 37:414–420.

Zheng J, Lin X, Lu Y. 2006. Stress analysis of plastic pipe reinforced by cross helically wound steel wires. Proceedings of the ASME 2006 pressure vessels and piping/ICPVT-11 conference; American Society of Mechanical Engineers Digital Collection.

Zhu Y. 2007. Buckling analysis of plastic pipe reinforced by winding steel wires under external pressure. Hangzhou City. Zhejiang University.

Appendix

(a) Detailed valid dimensions of specimens

Table A1. Detailed valid dimensions of #1 FGRFP.

#1					
Wall thickness (mm)		A	B	C	D
	1	13.32	13.52	12.40	13.02
	2	12.56	12.72	13.10	13.10
	Mean value		12.96		
	RSD		2.74%		

Outter diameter (mm)		AC		BD	
	1	76.32		76.04	
	2	76.94		76.44	
	Mean value		76.44		
	Initial Ovalization		0.51%		

Table A2. Detailed valid dimensions of #2 FGRFP.

#2					
Wall thickness (mm)		A	B	C	D
	1	13.26	13.58	13.42	13.00
	2	13.16	13.76	13.06	13.58
	Mean value		13.35		
	RSD		1.92%		

Outter diameter (mm)		AC		BD	
	1	76.62		76.10	
	2	76.62		76.98	
	Mean value		76.58		
	Initial Ovalization		0.10%		

Table A3. Detailed valid dimensions of #3 FGRFP.

#3					
Wall thickness (mm)		A	B	C	D
	1	12.90	12.74	12.38	13.24
	2	13.32	13.00	12.94	12.72
	Mean value		12.90		
	RSD		2.17%		

Outter diameter (mm)		AC		BD	
	1	76.70		76.12	
	2	77.00		77.02	
	Mean value		76.71		
	Initial Ovalization		0.36%		

(b) The proof of Equation 3
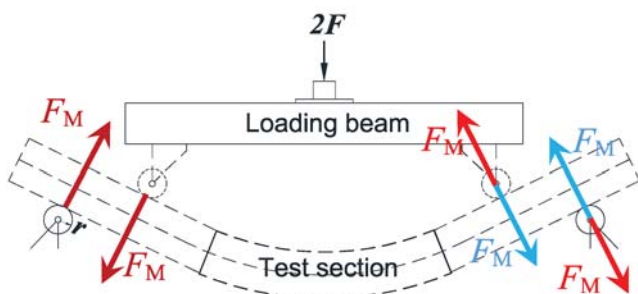
Figure A1. The force diagrams of the pipe wall and the roller.

There are some considerations needed to be noted.

(1) The pipe wall offers a supporting force (F_M) to the roller and direction of the force is perpendicular to the pipe wall of the rigid region.
(2) The direction of static friction force between the pipe wall and the roller is along the tangent direction of the edge of the roller. In addition, that force can make the roller to roll.
(3) Because the loading process is slow enough, the roller is in the equilibrium with any value of α and the roller is not rolling at a particular point in time. It means that there is no static friction force between the roller and the pipe wall at a particular point in time. (If there is static friction force between the roller and the pipe wall at a particular point in time, the roller will roll under the static friction force)
(4) There is no friction in the bearing of the roller.

Therefore, $F_M = \dfrac{F}{\cos \alpha}$.
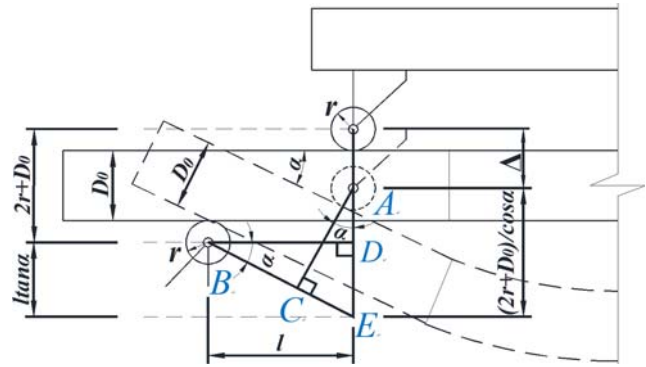
Figure A2. The proof of Equation 3.

It should be noted that the straight line BE is parallel to the rigid region of the bent specimen indicated by the dash line in Fig. A2 and the straight line BD is parallel to the rigid region of the initial specimen indicated by the solid line in Fig. A2. Hence, the included angle of BE and BD is equal to α.

(1) Known conditions:

$$AC = D_0 + 2r$$
$$BD = l$$

(2) Solutions:

$$\therefore \text{In the} \Delta ACE, CE = AC \cdot tan\alpha = (2r + D_0)tan\alpha$$

$$\text{In the } \Delta BDE, BE = \frac{BD}{\cos \alpha} = \frac{l}{\cos \alpha}$$

$$\therefore BC = \frac{l}{\cos \alpha} - (2r + D_0)tan\alpha$$

Bending moment exerted on the pipe can be expressed as:

$$M = F_M \cdot BC = \frac{F}{\cos \alpha} \cdot [\frac{l}{\cos \alpha} - (2r + D_0)tan\alpha].$$

(c) The detailed equation in section 3.2

Symbols used in Section 3.2 can be calculated by the following expression.

$$E_1 = (E_1^1, E_1^2, \cdots\cdots, E_1^k, \cdots\cdots, E_1^n) \tag{A1}$$

$$E_2 = (E_2^1, E_2^2, \cdots\cdots, E_2^k, \cdots\cdots, E_2^n) \tag{A2}$$

$$E_3 = (E_3^1, E_3^2, \cdots\cdots, E_3^k, \cdots\cdots, E_3^n) \tag{A3}$$

$$G_{12} = (G_{12}^1, G_{12}^2, \cdots\cdots, G_{12}^k, \cdots\cdots, G_{12}^n) \tag{A4}$$

$$G_{13} = (G_{13}^1, G_{13}^2, \cdots\cdots, G_{13}^k, \cdots\cdots, G_{13}^n) \tag{A5}$$

$$G_{23} = (G_{23}^1, G_{23}^2, \cdots\cdots, G_{23}^k, \cdots\cdots, G_{23}^n) \tag{A6}$$

$$\boldsymbol{\nu}_{12} = (\nu_{12}^1, \nu_{12}^2, \cdots\cdots, \nu_{12}^k, \cdots\cdots, \nu_{12}^n) \tag{A7}$$

$$\boldsymbol{\nu}_{13} = (\nu_{13}^1, \nu_{13}^2, \cdots\cdots, \nu_{13}^k, \cdots\cdots, \nu_{13}^n) \tag{A8}$$

$$\boldsymbol{\nu}_{23} = (\nu_{23}^1, \nu_{23}^2, \cdots\cdots, \nu_{23}^k, \cdots\cdots, \nu_{23}^n) \tag{A9}$$

$$\boldsymbol{E}_z = (E_z^1, E_z^2, \cdots\cdots, E_z^k, \cdots\cdots, E_z^n) \tag{A10}$$

$$\boldsymbol{E}_r = (E_r^1, E_r^2, \cdots\cdots, E_r^k, \cdots\cdots, E_r^n) \tag{A11}$$

$$\boldsymbol{E}_\theta = (E_\theta^1, E_\theta^2, \cdots\cdots, E_\theta^k, \cdots\cdots, E_\theta^n) \tag{A12}$$

$$\boldsymbol{E}_{PE} = (E_{PE}^1, E_{PE}^2, \cdots\cdots, E_{PE}^k, \cdots\cdots, E_{PE}^n) \tag{A13}$$

$$\boldsymbol{C} = (\boldsymbol{E}_1, \boldsymbol{E}_2, \boldsymbol{E}_3, \boldsymbol{G}_{12}, \boldsymbol{G}_{13}, \boldsymbol{G}_{23}, \boldsymbol{\nu}_{12}, \boldsymbol{\nu}_{13}, \boldsymbol{\nu}_{23}) \tag{A14}$$

The figures for modulus of the composite material depend on the specific value of the strain. To be more specific, Equations A1–A13 demonstrate the different modulus under various strain.

(d) Comparison between M_u^{MSTM} and M_u^{NSM}

Table A4. Comparison between modified STM and NSM with different outer diameters.

D(mm)	t(mm)	D/t	M_u^{MSTM} ($\times 10^6$N $\cdot$ mm)	M_u^{NSM} ($\times 10^6$N $\cdot$ mm)	Error (%)
65	13	5	1.23	1.26	2.44
78	13	6	1.89	1.89	1.00
91	13	7	2.65	2.61	0.99
104	13	8	3.49	3.42	0.98
117	13	9	4.38	4.31	0.98
130	13	10	5.41	5.40	1.00
143	13	11	6.28	6.30	1.00
156	13	12	7.24	7.42	1.02

Table A5. Comparison between modified STM and NSM with a constant D/t ratio.

D(mm)	t(mm)	D/t	M_u^{MSTM} ($\times 10^6$N $\cdot$ mm)	M_u^{NSM} ($\times 10^6$N $\cdot$ mm)	Error (%)
49.3	8.5	5.8	0.36	0.37	4.22
58.0	10.0	5.8	0.70	0.70	1.00
66.7	11.5	5.8	1.18	1.16	0.98
75.4	13.0	5.8	1.85	1.79	0.97
84.1	14.5	5.8	2.73	2.60	0.95
92.8	16.0	5.8	3.82	3.63	0.95
101.5	17.5	5.8	5.17	4.90	0.95
110.2	19.0	5.8	6.80	6.44	0.95

Table A6. Comparison between modified STM and NSM with different winding angles.

D(mm)	t(mm)	Winding angle(°)	M_u^{MSTM} ($\times 10^6$N $\cdot$ mm)	M_u^{NSM} ($\times 10^6$N $\cdot$ mm)	Error (%)
130	13	30	9.70	9.60	1.01
130	13	35	8.00	8.14	1.66
130	13	40	6.87	7.12	3.50
130	13	45	6.08	6.37	4.58
130	13	50	5.52	5.81	5.00
130	13	55	5.56	5.40	2.99
130	13	60	4.83	5.09	5.07
130	13	65	4.62	4.86	4.97
130	13	70	4.46	4.68	4.82

(e) Comparison between κ_u^{NSM} and $\hat{\kappa}_u$

Table A7. Comparison between κ_u^{NSM} and $\hat{\kappa}_u$ with different outer diameters.

D(mm)	t(mm)	D/t	κ_u^{NSM} (m^{-1})	$\hat{\kappa}_u$ (m^{-1})	Error (%)
65	13	5	4.80	4.80	0.03
78	13	6	3.40	3.40	0.09
91	13	7	2.52	2.53	0.56
104	13	8	1.92	1.96	2.17
117	13	9	1.57	1.56	0.42
130	13	10	1.43	1.27	10.98
143	13	11	1.08	1.06	2.41
156	13	12	0.88	0.89	1.03

Table A8. Comparison between κ_u^{NSM} and $\hat{\kappa}_u$ with a constant D/t ratio.

D(mm)	t(mm)	D/t	κ_u^{NSM} (m^{-1})	$\hat{\kappa}_u$ (m^{-1})	Error (%)
49.3	8.5	5.8	6.10	5.95	2.41
58.0	10.0	5.8	4.90	4.93	0.70
66.7	11.5	5.8	4.15	4.19	0.95
75.4	13.0	5.8	3.55	3.62	2.06
84.1	14.5	5.8	3.20	3.18	0.63
92.8	16.0	5.8	2.89	2.82	2.32
101.5	17.5	5.8	2.64	2.53	4.07
110.2	19.0	5.8	2.39	2.29	4.13